

pubs.acs.org/JACS Article

Multistep Crystallization of Dynamic Nanoparticle Superlattices in **Nonaqueous Solutions**

Yaxu Zhong, Vincent R. Allen, Jun Chen, Yi Wang, and Xingchen Ye*



Cite This: https://doi.org/10.1021/jacs.2c06535



Read Online

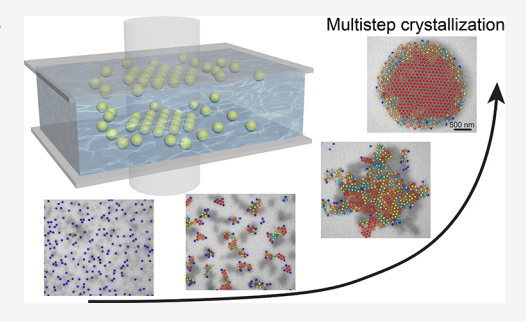
ACCESS I

Metrics & More

Article Recommendations

Supporting Information

ABSTRACT: Crystallization is a universal phenomenon underpinning many industrial and natural processes and is fundamental to chemistry and materials science. However, microscopic crystallization pathways of nanoparticle superlattices have been seldom studied mainly owing to the difficulty of real-time observation of individual self-assembling nanoparticles in solution. Here, using in situ electron microscopy, we directly image the full self-assembly pathway from dispersed nanoparticles into ordered superlattices in nonaqueous solution. We show that electron-beam irradiation controls nanoparticle mobility, and the solvent composition largely dictates interparticle interactions and assembly behaviors. We uncover a multistep crystallization pathway consisting of four distinct stages through multi-order-parameter analysis and visualize the formation, migration, and



annihilation of multiple types of defects in nanoparticle superlattices. These findings open the door for achieving independent control over imaging conditions and nanoparticle assembly conditions and will enable further study of the microscopic kinetics of assembly and phase transition in nanocolloidal systems.

■ INTRODUCTION

Crystallization is a universal phenomenon underpinning many natural processes and research practices. 1-3 The classical nucleation theory assumes that nucleation can be described by one reaction coordinate and that all relevant order parameters change simultaneously during crystallization. 4 Yet, nonclassical pathways of crystallization have been predicted by computer simulation⁵⁻⁸ and observed experimentally in many systems including protein crystallization, mineralization, and selfassembly of micrometer-sized colloids 10-12 and nanoparticles. 13 At the nanoscale, discreteness of matter can give rise to emergent nonadditivity and many-body effects, which are generally not accounted for by existing theories. 14 Consequently, the microscopic pathways and dynamics of nanoparticle assembly can be difficult to predict, even if the pairwise interaction potentials are known. Direct observation of these kinetic pathways will help to refine existing models and advance our ability to create nanoscale assemblies with desired properties. Unlike small-angle X-ray scattering, which probes the ensemble in reciprocal space, 15 or optical microscopy techniques, which lack sufficient spatial resolution to image nanoparticles, in situ liquid cell transmission electron microscopy (LCTEM) is a powerful technique capable of capturing nanoscale dynamics with high spatiotemporal resolution. 13,16-21 LCTEM studies on nanoparticle assembly thus far have primarily focused on aqueous solutions. 13,18,22-25 In nonaqueous media, markedly reduced particle mobility or small-scale assemblies were usually observed, 21,26-30 although the exact cause remains elusive.

Here, we utilize nonaqueous LCTEM and exploit the impinging electrons to controllably initiate and image nanoparticle assembly with single-particle resolution. Distinct from prior LCTEM works on nanoparticle assembly, we demonstrate that the solvent plays a central role in determining the interaction potential between nanoparticles and their selfassembly behavior. We construct a statistical map of the evolution from individual nanoparticles to long-range-ordered superlattices using local and global order parameters. The microscopic pathway to crystallization involves multiple intermediate states, a hallmark of nonclassical crystallization. Our findings demonstrate that diverse and sometimes unexpected pathways exist for achieving structural ordering at the nanoscale, and open new opportunities for elucidating complex mechanisms of nanoparticle self-assembly in nonaqueous solutions.

RESULTS AND DISCUSSION

The motion and assembly of gold nanospheres suspended in different nonaqueous solvents were imaged using LCTEM, as illustrated schematically in Figure 1a. We grafted gold nanospheres (68.1 nm in diameter) with thiol-terminated

Received: June 21, 2022



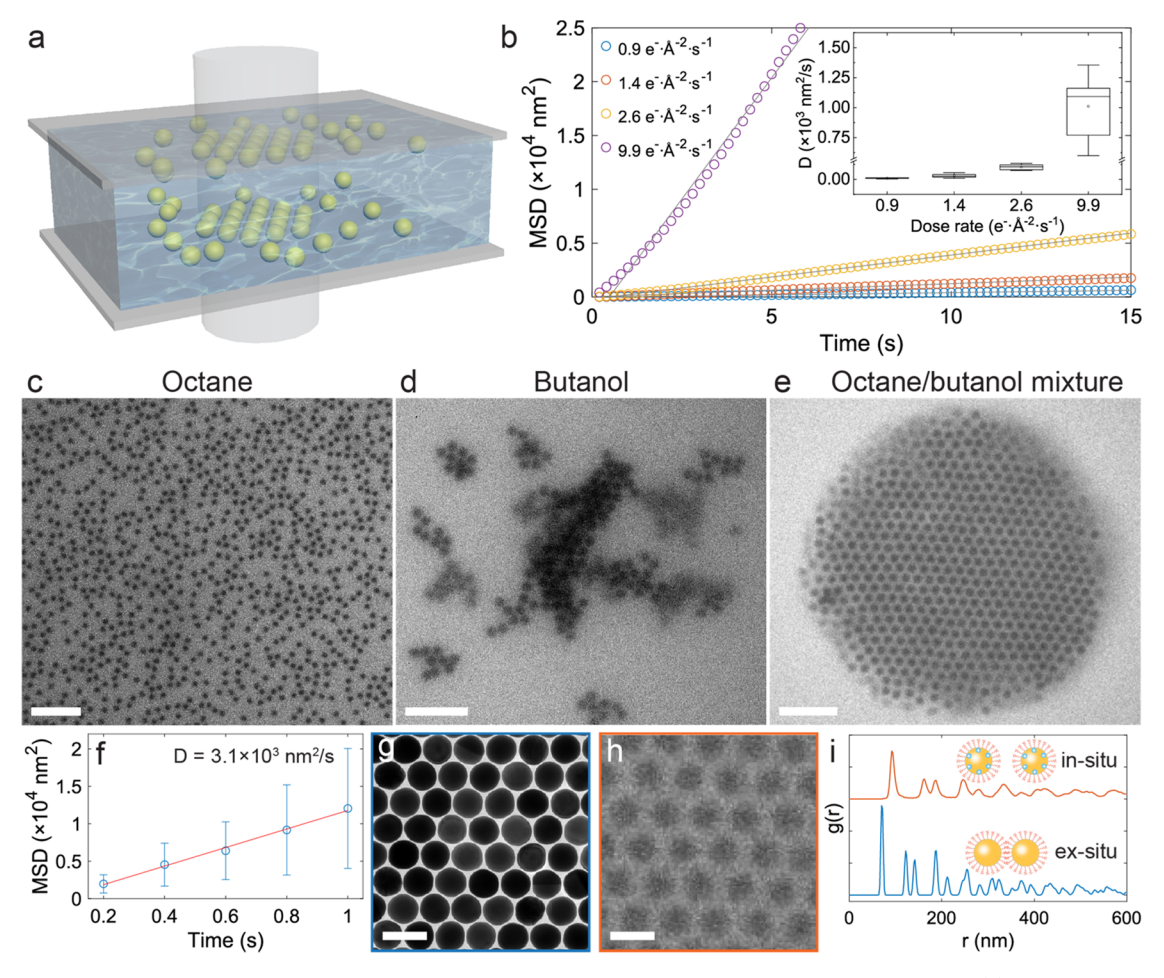


Figure 1. Controlling the self-assembly behavior of gold nanoparticles in LCTEM through the choice of solvent. (a) Scheme showing the self-assembly of gold nanoparticles near the Si_3N_4 membrane windows under electron-beam irradiation. (b) MSD plots and diffusion constants of gold nanoparticles in octane under different electron dose rates. (c-e) Exemplary LCTEM images showing distinct self-assembly behaviors in different solvents: (c) dispersion in octane, (d) aggregation in butanol, and (e) crystallization in a 1:1 (v/v) mixture of octane and butanol. (f) MSD plot of gold nanoparticles in 1:1 (v/v) octane/butanol mixture based on particle tracking results at the early stage of crystallization. (g-i) Representative high-magnification TEM images (g, h) and corresponding g(r) plots (i) for 2D hexagonal superlattices obtained from ex situ drying-mediated assembly (g) and in situ LCTEM (h) using the same gold nanoparticles. Scale bars: (c-e) 500 nm and (g, h) 100 nm.

polystyrene ($M_{\rm w}$ = 3.2 kDa) via ligand exchange to prevent their irreversible aggregation under LCTEM conditions (Figure S1a and Supporting Notes 1 and 2). Before TEM imaging, gold nanospheres had adsorbed onto the Si₃N₄ windows and become immobile. However, they began to move within seconds of electron-beam irradiation and exhibited a quasi-two-dimensional Brownian motion under low-dose (<10.0 $e^-{\cdot}\mathring{A}^{-2}{\cdot}s^{-1})$ imaging conditions (Supporting Movie 1). Mean squared displacement analysis of nanospheres in the field-of-view revealed that particle mobility in octane increased monotonically with the electron dose rate (Figures 1b and S2 and Supporting Note 3). At high dose rates (≥ 20.0 $e^{-}\cdot A^{-2}\cdot s^{-1}$), nanospheres quickly desorbed from the vicinity of the Si₃N₄ window and later departed from the imaging area, suggesting strong repulsion between diffusing nanoparticles and the window. We attribute the observed dose-ratedependent mobility to electron-beam-induced positive charging of Si₃N₄ windows and gold nanospheres, which has been postulated to cause nanoparticle mobility in aqueous LCTEM studies. 22,24,31-33 Here, the weak dielectric screening in nonaqueous media further reduces the adhesion between nanospheres and Si₃N₄ windows, giving rise to diffusivity exceeding 10³ nm²·s⁻¹ at low dose rates.

The interactions and self-assembly behaviors of gold nanospheres depend sensitively on the solvent composition (Figure 1c-e and Supporting Movie 2). At the dose rate of 3.1 e-A-2·s-1, gold nanospheres were mobile but remained dispersed in octane (dielectric constant $\varepsilon = 1.95$; Figures 1c and S3). By contrast, they coagulated into disordered aggregates reminiscent of diffusion-limited structures in butanol (ε = 17.84; Figures 1d and S4). These observations suggest that the interaction between gold nanospheres is longrange-repulsive in octane, but switches to being strongly attractive in a more polar solvent. Therefore, we hypothesize that by tailoring the solvent composition, one could tune the particle interaction to be moderately attractive and favor crystallization rather than aggregation. To test this hypothesis, we used a mixture of octane/butanol (v/v = 1:1) for LCTEM under otherwise identical conditions. As shown in Figure 1e, gold nanospheres crystallized into a well-ordered two-dimensional (2D) superlattice. The sparse population of nanoparticles beyond the superlattice suggests that the assembly is caused by attractions among nanoparticles, which is different from a Kirkwood-Alder-type transition.³⁴ The diffusivity of nanoparticles reached $3.1 \times 10^3 \text{ nm}^2 \cdot \text{s}^{-1}$ (Figure 1f), which is among the highest attained with LCTEM despite being 3

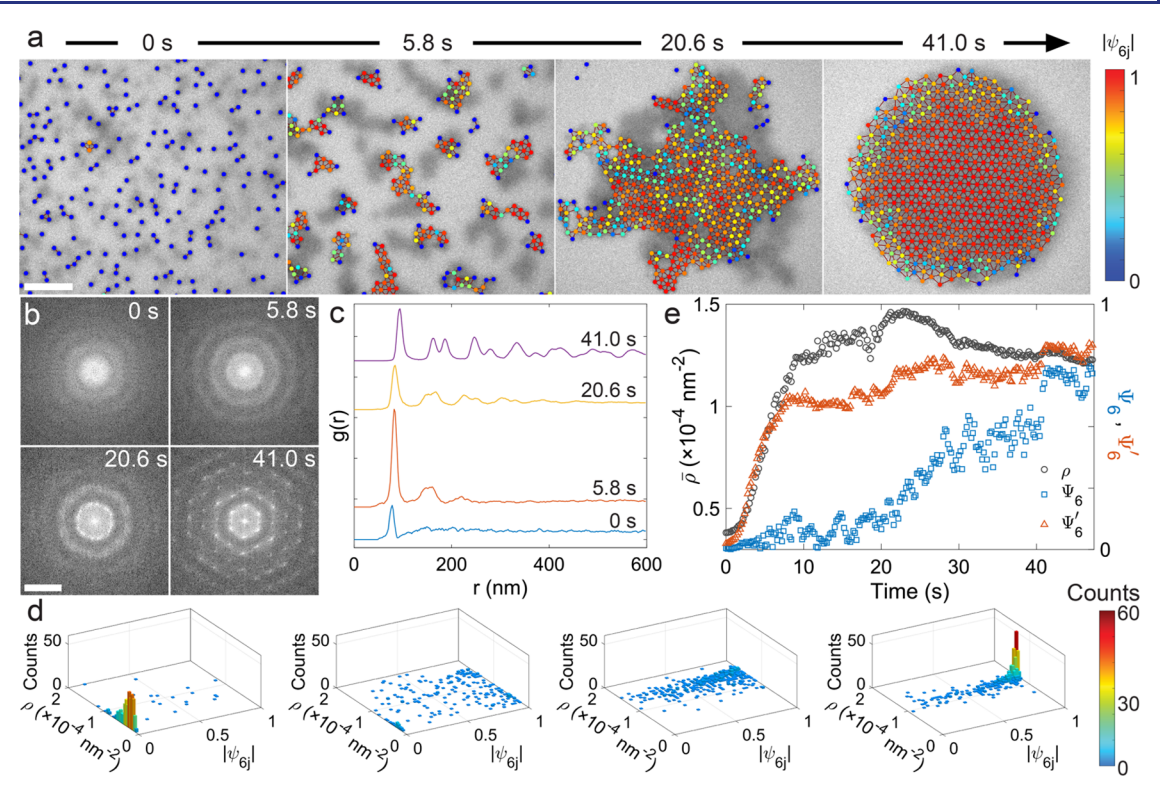


Figure 2. Multistep crystallization of nanoparticle superlattices. (a, b) Time-lapse LCTEM images overlaid with particle centroids (a) and corresponding FFT patterns (b). The nanoparticle centroids in (a) are color-coded according to the modulus of 6-fold bond-orientational order parameters ($|\psi_{6j}|$). All nearest-neighbors are connected. (c) Plots of g(r) at different stages. (d) Order-density 2D histograms ($|\psi_{6j}|$, ρ) for the four stages shown in panel (a). (e) Plots of local density $(\overline{\rho})$ and global 6-fold bond-orientational order parameters ($\Psi_6 = |\langle \psi_{6j} \rangle|$ and $\Psi'_6 = \langle |\psi_{6j}| \rangle$) versus time. Scale bars: (a) 500 nm and (b) 1/200 nm⁻¹.

orders of magnitude smaller than that predicted by the Stokes–Einstein relation (Table S1). Crucially, the average nearest-neighbor surface-to-surface distance (~25 nm) of the in situ formed 2D superlattice far exceeds that of the superlattice formed ex situ by drying-mediated assembly or the estimated polystyrene ligand shell thickness (<3 nm) in octane/butanol (v/v = 1:1) (Figure 1g–i). These results indicate that long-range interactions drive the assembly of charged gold nanospheres under current LCTEM conditions and that ligand—ligand interactions are insignificant in stabilizing superlattices in situ.

To gain quantitative insights, we estimated pairwise interactions between gold nanospheres (Supporting Note 4). Although the exact charge number per nanoparticle and the ionic strength of solution under electron irradiation are difficult to measure directly, plausible combinations of particle charge and Debye length could still be identified by considering the outcomes of self-assembly. For example, assuming 200 charges per particle and a Debye length of 5.5 nm in octane/butanol (v/v = 1:1), the total pairwise interaction between gold nanospheres shows a secondary minimum U_1 of -0.51 kT at the center-to-center distance of 94.5 nm followed by an energy barrier U_2 of 6.0 kT at a shorter distance (Figure S5). After performing an extensive parametric analysis using different cutoff values of U1 and U2, we are able to locate a range of combinations of Debye lengths (~3 to 8 nm) and charges per nanosphere (~100 to 400) that could explain the in situ formation of 2D superlattices (Figures S6 and S7).35 Notably, the retrieved charge numbers are 1 order of magnitude smaller than previously reported values for similarly sized gold nanocrystals capped with charged ligands. 13 Meanwhile, the

Debye lengths seem reasonable given the lower dielectric constants of organic solvents than water.

Accurate segmentation of individual nanoparticles from LCTEM video frames is fundamental to elucidate self-assembly dynamics. Conventional methods yield poor results because of the low signal-to-noise ratio of raw LCTEM images and inhomogeneous background arising from out-of-focus nanoparticles assembling near the other Si₃N₄ window (Figure S8). To overcome this challenge, we applied deep learning-based approaches to improve the accuracy and throughput of image segmentation (Figures S9-S11 and Supporting Note 5).³⁶⁻ Specifically, a convolutional neural network named U-net was trained with a dataset consisting of 600 image pairs generated by augmentation of three precisely annotated LCTEM images.³⁶ Afterward, particle centroids were extracted from the segmented LCTEM images, and multiple order parameters such as 6-fold bond-orientational order parameter (ψ_{6i}) and density (ρ , defined as the reciprocal of the Voronoi cell area) were computed (Figures S10-S13). 12,39

The assembly of gold nanospheres into 2D superlattices followed a multistep crystallization pathway (Figures 2 and S14 and Supporting Movie 3). Four distinct stages were identified, namely, gas state, cluster state, polycrystalline, and single-crystalline solid states at 0, 5.8, 20.6, and 41.0 s, respectively (Figure 2a). Diffuse rings were observed in the fast Fourier transform (FFT) patterns before 20.0 s, indicative of the absence of long-range translational symmetry (Figure 2b). By contrast, sharp diffraction spots of hexagonal symmetry were found at a later stage (e.g., 41.0 s) signifying long-range crystalline order. Radial distribution function g(r) analysis reveals the emergence of long-range order: High-order peaks

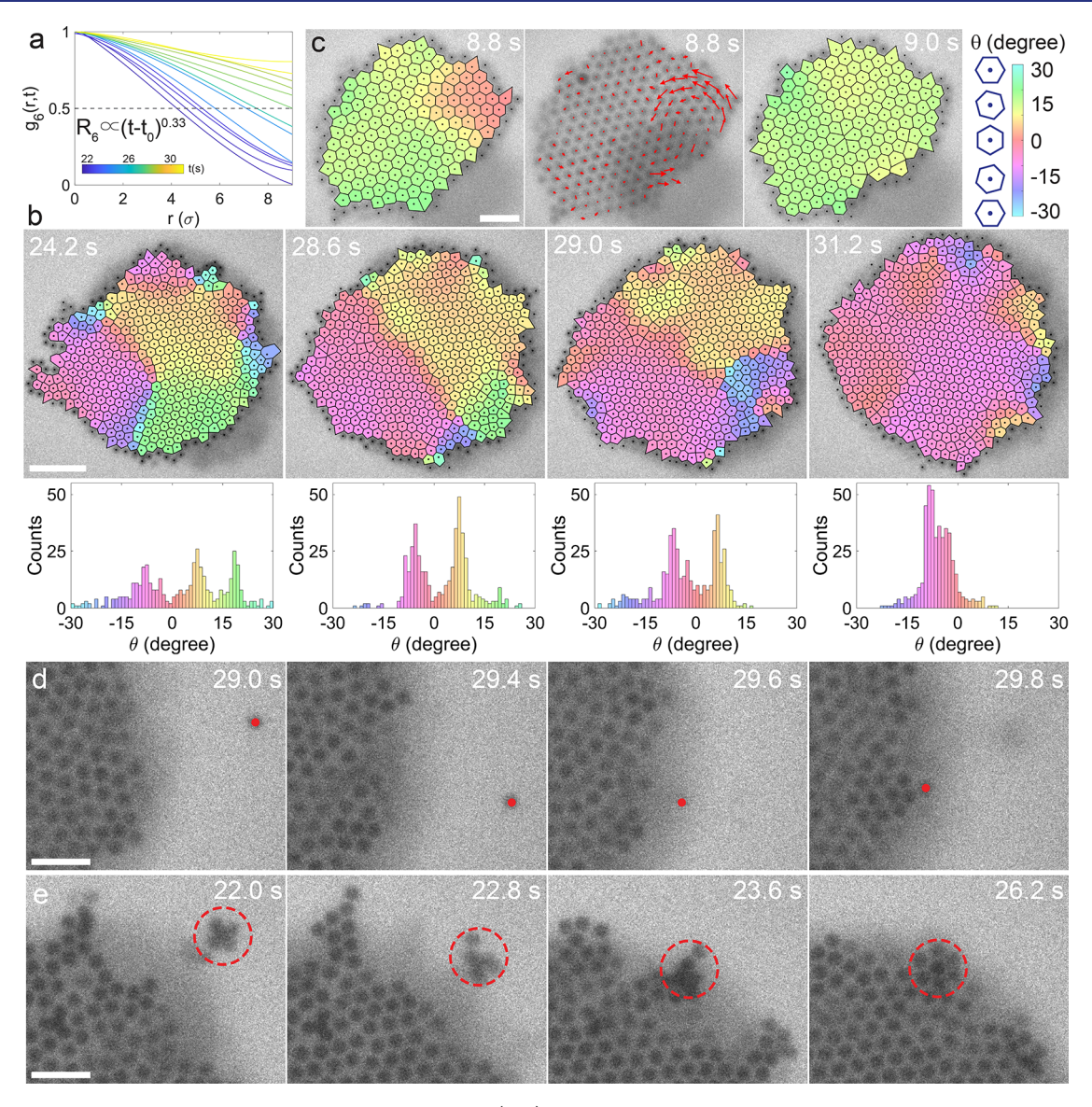


Figure 3. Structural transitions at different stages of crystallization. (a, b) Kinetics of grain growth and pathways of grain boundary removal during the transition from polycrystalline solid to single-crystalline superlattices. (a) Evolution of 6-fold bond-orientational correlation function $g_6(r,t)$ and the characteristic grain size R_6 (retrieved by setting $g_6(R_6,t)=0.5$). (b) Dynamics of high-angle and low-angle grain boundary migrations during the transition from polycrystalline to single-crystalline superlattices. The Voronoi cells are color-coded according to the smoothed local crystalline orientation (θ) calculated from the argument of $\overline{\psi}_{6j}$ using $\theta=1/6\arg(\overline{\psi}_{6j})$, with the corresponding histogram shown below each micrograph. (c) Grain boundary elimination through grain rotation during crystallization of gold octahedra into superlattices. (d) Monomer attachment and (e) cluster attachment to a large growing domain during crystallization. Scale bars: (b) 500 nm and (c-e) 200 nm.

gradually develop, which is accompanied by peak shifts toward larger distances (Figure 2c). The distinct stages of crystallization were further manifested in 2D histograms of local parameters ρ and $|\psi_{6j}|$ (Figure 2d). For the gas state, most nanoparticles exhibit low density ($\rho<1\times10^{-4}~\rm nm^{-2})$ and low bond-orientational order ($|\psi_{6j}|<0.5$). The state of cluster formation, however, is characterized by broad distributions of ρ and $|\psi_{6j}|$. Furthermore, the polycrystalline solid-state features narrowly distributed high densities and broadly distributed $|\psi_{6j}|$, whereas simultaneously high ρ and $|\psi_{6j}|$ values are found for the single-crystalline solid state.

To quantify and understand the evolution of global order during superlattice formation, we used three order parameters: average density $\overline{\rho}$ and two global 6-fold bond-orientational order parameters defined as $\Psi_6 = |\langle \psi_{6j} \rangle|$ and $\Psi_6' = \langle |\psi_{6j}| \rangle$ (Figure 2e). 26,40 Ψ_6 characterizes long-range translational

symmetry by retaining the phase information of local ψ_{6i} values, whereas Ψ_6' better informs short-range translational order. From 0 to 9.0 s, both $\overline{\rho}$ and Ψ_6' increased rapidly due to cluster formation and growth. Meanwhile, Ψ_6 barely increased, suggesting random orientations of the clusters. From 9.0 to 20.6 s, $\overline{\rho}$ continued to increase slowly owing to cluster coalescence, with relatively high Ψ'_6 (~0.6), yet low Ψ_6 (~0.2) indicating a polycrystalline structure. After 20.6 s, Ψ_6 started to increase as a result of grain growth and development of medium-range translational order. Meanwhile, Ψ_6' increased slightly because of abundance of structural defects at grain boundaries. Intriguingly, $\overline{\rho}$ started to decrease after reaching its peak at 23.2 s, indicating lattice expansion while retaining hexagonal order. The weak correlations among these order parameters and the fact that densification precedes structural ordering signify a multistep crystallization pathway of 2D

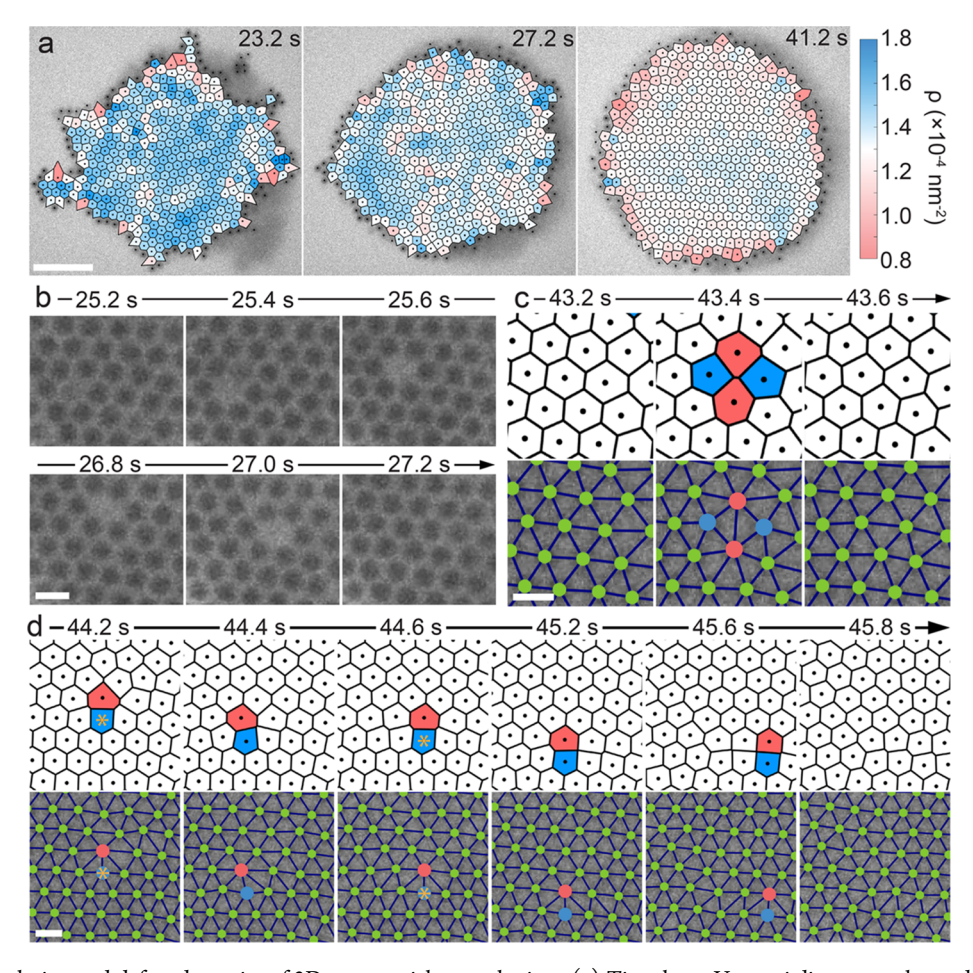


Figure 4. Density evolution and defect dynamics of 2D nanoparticle superlattices. (a) Time-lapse Voronoi diagrams color-coded according to local density. (b) Time-lapse LCTEM images showing vacancy generation and diffusion in a hexagonal superlattice. (c, d) Dislocation dynamics in 2D nanoparticle superlattices. (c) Generation and annihilation of a dislocation pair. (d) Diffusion of dislocation by glide and climb. The Voronoi diagrams (top row) and Delaunay triangulation plots (bottom row) are color-coded according to local coordination number (blue for 5, white/green for 6, and red for 7). The position of vacancy formation that leads to subsequent dislocation climb is indicated by a yellow asterisk. Scale bars: (a) 500 nm and (b–d) 100 nm.

nanoparticle superlattices (Figure 2d). To establish generality, we also studied the self-assembly behavior of gold nano-octahedra under similar LCTEM conditions (Figure S1b). Individual octahedra exhibited rapid rotation and thus appeared as spherical objects in LCTEM images (Supporting Movie 4). Initially dispersed nanooctahedra self-assembled into a 2D hexagonal rotator phase 6,41 in octane/butanol (v/v = 1:1) following an analogous multistep crystallization pathway as gold nanospheres (Figures S15 and S16).

We further examined the microscopic details underlying transitions between different stages of crystallization. Upon electron-beam irradiation, sparsely distributed nanoparticles that were mostly monomers assembled into a mixture of dimers, trimers, and oligomers (Figure S17, $t=0.8~\rm s$), which then transformed into small clusters with a concomitant depletion of monomers ($t=2.8~\rm s$). These small clusters appeared to be metastable, fluctuating between crystal-like and liquid-like structures and transferring monomers to form large clusters. The coalescence of large clusters yielded one connected yet poorly crystalline grain ($t=20.6~\rm s$) from which a large single-crystalline domain developed.

The kinetics of grain growth from polycrystalline to single-crystalline state was quantified using the 6-fold bond-orientational correlation function $g_6(r, t)$. A characteristic

grain size R_6 is obtained by setting $g_6(R_6, t) = 0.5$ (Supporting Note 6). 42,43 R_6 increased with time, indicating the growing extent of hexagonal bond-orientational order. The time dependence of R_6 is best fitted by $R_6 \sim (t - t_0)^{0.33}$ (Figures 3a and \$18). An exponent smaller than 0.5 indicates abnormal grain growth. 42 Such anomalous grain-growth behaviors have been reported for micrometer-sized colloidal crystals, which may arise from stress-assisted grain growth, grain rotation, and microstructures of grain boundaries.⁴² Voronoi tessellation color-coded according to the smoothed local crystalline orientation (θ) revealed crystalline domains with curved rough boundaries (Figure 3b and Supporting Movie 5). Here, θ is calculated from the argument of the coarse-grained local 6-fold bond-orientational order parameter $\overline{\psi}_{6j}$ and θ = 1/ $6\arg(\overline{\psi}_{6i})$. The histogram of θ -values for the polycrystalline state shows the coexistence of high-angle (>15°) and low-angle (<15°) grain boundaries (Figure 3b, t = 24.2 s). The highangle grain boundary was removed more rapidly than lowangle ones likely caused by high interfacial energies associated with large grain misorientations. 42 In addition to grain boundary migration through local rearrangement of particles (Figures 3b and S19 and Supporting Movie 5), we observed another mode of grain boundary elimination-grain rotation. 44,45 Specifically, rotation of a small domain within a

polycrystalline superlattice removed the low-angle grain boundary producing a single-crystalline superlattice (Figure 3c). The instantaneous velocity map shows that grain rotation took place through tangential motion along the curved grain boundary (Figure 3c and Supporting Movie 6). Furthermore, assemblies can grow by incorporating fresh nanoparticles into existing domains. Both monomer attachment and cluster attachment were observed followed by lattice rearrangement, demonstrating the pathway complexity of grain growth in nanoparticle assembly (Figures 3d,e, S20 and S21 and Supporting Movie 7). From 23.2 to 47.4 s, the average local density dropped by ~15% (Figure 4a and Supporting Movie 8). We attribute this nonintuitive lattice expansion to a growing number of electrostatic charges per particle under continuous electron-beam irradiation, weakening the overall attraction between nanoparticles.

The dynamic nature of 2D hexagonal superlattices and the LCTEM imaging approach enable us to visualize the formation, migration, and annihilation of structural defects (Supporting Note 7). Defects such as vacancies, disclinations, and dislocations play critical roles in determining the phase behavior and mechanical and rheological properties of colloidal crystals, 3,46,47 yet the steps underlying the dynamics of such defects are rarely studied for nanoparticle superlattices. As illustrated in Figure 4b, a monovacancy was generated, diffused along the symmetry axes of the hexagonal lattice, and eventually vanished after reaching either grain boundaries or the periphery of the superlattice (Figure S22a and Supporting Movie 9). The dislocation core in a 2D hexagonal lattice consists of neighboring 5-fold and 7-fold coordinated particles, which can be visualized by Voronoi tessellation and Delaunay triangulation. Shown in Figure 4c is an example of generation of a bound dislocation pair with equal and opposite Burgers vectors followed by its annihilation, analogous to the Stone-Wales transformation and its reverse process in graphene (Figure S22b,c and Supporting Movie 10).⁴⁸ Dislocations can migrate through either glide or climb mechanism (Figure S23a,b). Dislocation glide involves particle rearrangements around the dislocation core, whereas dislocation climb is a nonconservative process and usually requires vacancy formation near the dislocation core. 44,49 Moreover, two dislocations with $\sim 120^{\circ}$ between their Burgers vectors in a hexagonal lattice reacted to form a single dislocation while preserving the net Burgers vector (Figure S23c).⁴⁴ We also identified pathways of dislocation annihilation in the 2D nanoparticle superlattice (Figure 4d and Supporting Movie 11). The dislocation diffused to the periphery of the superlattice through a series of glide and climb steps, which restored the translational order of the hexagonal lattice.

CONCLUSIONS

In summary, we demonstrate a model material system, namely, polymer-grafted metal nanocrystals suspended in nonaqueous solvents, for studying self-assembly of nanoparticles into highly ordered superlattices using in situ LCTEM. Through systematic dose-rate-dependent experiments, we establish that electron-beam irradiation activates nanoparticle motion and largely controls nanoparticle mobility, while the solvent composition mediates nanoparticle interaction and dictates their assembly pathways. Nanoparticle diffusivities as high as $3.1 \times 10^3 \ \mathrm{nm}^2 \cdot \mathrm{s}^{-1}$ were attained under low-dose imaging conditions. These advances bring us one step closer toward independent control of LCTEM imaging conditions and

particle self-assembly conditions. We capture and analyze the full self-assembly pathway from individual nanoparticles to 2D hexagonal superlattices, facilitated by newly developed deep learning-based image segmentation methods. We identify a multistep crystallization pathway characterized by four distinct stages and observed in real-time defect dynamics in 2D nanoparticle superlattices. Our work not only illustrates the complex and often poorly understood microscopic pathways of crystallization in self-assembling nanoparticles but also paves the way for studying crystallization in multicomponent nanoparticle systems as well as phase transition kinetics in nanoparticle assemblies using LCTEM.

ASSOCIATED CONTENT

Supporting Information

The Supporting Information is available free of charge at https://pubs.acs.org/doi/10.1021/jacs.2c06535.

Motions of gold nanospheres in octane under different electron dose rates (MOV)

Solvent-dependent self-assembly behaviors of gold nanospheres (MOV)

LCTEM movie showing multistep crystallization of gold nanospheres and synchronized data analysis results (MOV)

LCTEM movie showing multistep crystallization of gold octahedra and synchronized data analysis results (MOV) Grain boundary migration at a later stage of crystallization (MOV)

Grain boundary elimination through grain rotation (MOV)

Growth of nanoparticle superlattices by monomer attachment and cluster attachment (MOV)

Evolution of local densities of 2D nanoparticle superlattices (MOV)

Vacancy formation and diffusion in 2D nanoparticle superlattices (MOV)

Dislocation dynamics in 2D nanoparticle superlattices (MOV)

Long-time dislocation dynamics in 2D nanoparticle superlattices (MOV)

Detailed experimental methods; deep learning-based TEM image segmentation; quantitative analysis of nanoparticle duffusion and self-assembly; calculations of nanoparticle pairwise interactions; additional discussions on defect dynamics of 2D nanoparticle superlattices; Figures S1–S23; and Table S1 (PDF)

AUTHOR INFORMATION

Corresponding Author

Xingchen Ye — Department of Chemistry, Indiana University, Bloomington, Indiana 47405, United States; ⊚ orcid.org/ 0000-0001-6851-2721; Email: xingye@indiana.edu

Authors

Yaxu Zhong – Department of Chemistry, Indiana University, Bloomington, Indiana 47405, United States

Vincent R. Allen – Department of Chemistry, Indiana University, Bloomington, Indiana 47405, United States Jun Chen – Department of Chemistry, Indiana University,

Bloomington, Indiana 47405, United States; oorcid.org/

Yi Wang – Department of Chemistry, Indiana University, Bloomington, Indiana 47405, United States

Complete contact information is available at: https://pubs.acs.org/10.1021/jacs.2c06535

Notes

The authors declare no competing financial interest.

ACKNOWLEDGMENTS

X.Y. acknowledges support from the US National Science Foundation through award DMR-2102526. Y.Z. acknowledges support from the College of Arts and Sciences Dissertation Research Fellowship at Indiana University. We thank the Indiana University Nanoscale Characterization Facility and the Electron Microscopy Center for access to instrumentation.

REFERENCES

- (1) Damasceno, P. F.; Engel, M.; Glotzer, S. C. Predictive self-assembly of polyhedra into complex structures. *Science* **2012**, 337, 453–457.
- (2) De Yoreo, J. J.; Gilbert, P. U. P. A.; Sommerdijk, N. A. J. M.; Penn, R. L.; Whitelam, S.; Joester, D.; Zhang, H.; Rimer, J. D.; Navrotsky, A.; Banfield, J. F.; Wallace, A. F.; Michel, F. M.; Meldrum, F. C.; Cölfen, H.; Dove, P. M. Crystallization by particle attachment in synthetic, biogenic, and geologic environments. *Science* **2015**, 349, No. aaa6760.
- (3) Li, B.; Zhou, D.; Han, Y. Assembly and phase transitions of colloidal crystals. *Nat. Rev. Mater.* **2016**, *1*, 15011.
- (4) Kelton, K. F. Crystal Nucleation in Liquids and Glasses. In *Solid State Physics*, Ehrenreich, H.; Turnbull, D., Eds.; Academic Press, 1991; Vol. 45, pp 75–177.
- (5) ten Wolde, P. R.; Frenkel, D. Enhancement of protein crystal nucleation by critical density fluctuations. *Science* **1997**, 277, 1975–1978.
- (6) Agarwal, U.; Escobedo, F. A. Mesophase behaviour of polyhedral particles. *Nat. Mater.* **2011**, *10*, 230–235.
- (7) Russo, J.; Tanaka, H. Nonclassical pathways of crystallization in colloidal systems. MRS Bull. **2016**, 41, 369–374.
- (8) Lee, S.; Teich, E. G.; Engel, M.; Glotzer, S. C. Entropic colloidal crystallization pathways via fluid—fluid transitions and multidimensional prenucleation motifs. *Proc. Natl. Acad. Sci. U.S.A.* **2019**, *116*, 14843—14851.
- (9) Sauter, A.; Roosen-Runge, F.; Zhang, F.; Lotze, G.; Jacobs, R. M. J.; Schreiber, F. Real-time observation of nonclassical protein crystallization kinetics. *J. Am. Chem. Soc.* **2015**, *137*, 1485–1491.
- (10) Savage, J. R.; Dinsmore, A. D. Experimental evidence for twostep nucleation in colloidal crystallization. *Phys. Rev. Lett.* **2009**, *102*, No. 198302.
- (11) Zhang, T. H.; Liu, X. Y. How does a transient amorphous precursor template crystallization. *J. Am. Chem. Soc.* **2007**, *129*, 13520–13526.
- (12) Tan, P.; Xu, N.; Xu, L. Visualizing kinetic pathways of homogeneous nucleation in colloidal crystallization. *Nat. Phys.* **2014**, *10*, 73–79.
- (13) Ou, Z.; Wang, Z.; Luo, B.; Luijten, E.; Chen, Q. Kinetic pathways of crystallization at the nanoscale. *Nat. Mater.* **2020**, *19*, 450–455.
- (14) Batista, C. A. S.; Larson, R. G.; Kotov, N. A. Nonadditivity of nanoparticle interactions. *Science* **2015**, *350*, No. 1242477.
- (15) Li, T.; Senesi, A. J.; Lee, B. Small angle X-ray scattering for nanoparticle research. *Chem. Rev.* **2016**, *116*, 11128–11180.
- (16) Liao, H.-G.; Zherebetskyy, D.; Xin, H.; Czarnik, C.; Ercius, P.; Elmlund, H.; Pan, M.; Wang, L.-W.; Zheng, H. Facet development during platinum nanocube growth. *Science* **2014**, 345, 916–919.
- (17) Park, J.; Elmlund, H.; Ercius, P.; Yuk, J. M.; Limmer, D. T.; Chen, Q.; Kim, K.; Han, S. H.; Weitz, D. A.; Zettl, A.; Alivisatos, A. P.

- 3D structure of individual nanocrystals in solution by electron microscopy. *Science* **2015**, 349, 290–295.
- (18) Ross, F. M. Opportunities and challenges in liquid cell electron microscopy. *Science* **2015**, *350*, No. aaa9886.
- (19) Ye, X.; Jones, M. R.; Frechette, L. B.; Chen, Q.; Powers, A. S.; Ercius, P.; Dunn, G.; Rotskoff, G. M.; Nguyen, S. C.; Adiga, V. P.; Zettl, A.; Rabani, E.; Geissler, P. L.; Alivisatos, A. P. Single-particle mapping of nonequilibrium nanocrystal transformations. *Science* **2016**, 354, 874–877.
- (20) Loh, N. D.; Sen, S.; Bosman, M.; Tan, S. F.; Zhong, J.; Nijhuis, C. A.; Král, P.; Matsudaira, P.; Mirsaidov, U. Multistep nucleation of nanocrystals in aqueous solution. *Nat. Chem.* **2017**, *9*, 77–82.
- (21) Sutter, P.; Sutter, E. Real-time electron microscopy of nanocrystal synthesis, transformations, and self-assembly in solution. *Acc. Chem. Res.* **2021**, *54*, 11–21.
- (22) Liu, Y.; Lin, X. M.; Sun, Y.; Rajh, T. In situ visualization of self-assembly of charged gold nanoparticles. *J. Am. Chem. Soc.* **2013**, *135*, 3764–3767.
- (23) Chen, Q.; Cho, H.; Manthiram, K.; Yoshida, M.; Ye, X.; Alivisatos, A. P. Interaction potentials of anisotropic nanocrystals from the trajectory sampling of particle motion using in situ liquid phase transmission electron microscopy. *ACS Cent. Sci.* **2015**, *1*, 33–39.
- (24) Woehl, T. J.; Prozorov, T. The mechanisms for nanoparticle surface diffusion and chain self-assembly determined from real-time nanoscale kinetics in liquid. *J. Phys. Chem. C* **2015**, *119*, 21261–21269.
- (25) Liu, C.; Ou, Z.; Guo, F.; Luo, B.; Chen, W.; Qi, L.; Chen, Q. "Colloid—atom duality" in the assembly dynamics of concave gold nanoarrows. *J. Am. Chem. Soc.* **2020**, *142*, 11669—11673.
- (26) Park, J.; Zheng, H.; Lee, W. C.; Geissler, P. L.; Rabani, E.; Alivisatos, A. P. Direct observation of nanoparticle superlattice formation by using liquid cell transmission electron microscopy. *ACS Nano* **2012**, *6*, 2078–2085.
- (27) Sutter, E.; Sutter, P.; Tkachenko, A. V.; Krahne, R.; de Graaf, J.; Arciniegas, M.; Manna, L. In situ microscopy of the self-assembly of branched nanocrystals in solution. *Nat. Commun.* **2016**, *7*, No. 11213.
- (28) Powers, A. S.; Liao, H. G.; Raja, S. N.; Bronstein, N. D.; Alivisatos, A. P.; Zheng, H. Tracking nanoparticle diffusion and interaction during self-sssembly in a liquid cell. *Nano Lett.* **2017**, *17*, 15–20.
- (29) Lee, J.; Nakouzi, E.; Song, M.; Wang, B.; Chun, J.; Li, D. Mechanistic understanding of the growth kinetics and dynamics of nanoparticle superlattices by coupling interparticle forces from real-time measurements. *ACS Nano* **2018**, *12*, 12778–12787.
- (30) Cepeda-Perez, E.; Doblas, D.; Kraus, T.; de Jonge, N. Electron microscopy of nanoparticle superlattice formation at a solid-liquid interface in nonpolar liquids. *Sci. Adv.* **2020**, *6*, No. eaba1404.
- (31) White, E. R.; Mecklenburg, M.; Shevitski, B.; Singer, S. B.; Regan, B. C. Charged nanoparticle dynamics in water induced by scanning transmission electron microscopy. *Langmuir* **2012**, 28, 3695–3698
- (32) Verch, A.; Pfaff, M.; de Jonge, N. Exceptionally slow movement of gold nanoparticles at a solid/liquid interface investigated by scanning transmission electron microscopy. *Langmuir* **2015**, *31*, 6956–6964.
- (33) Chee, S. W.; Baraissov, Z.; Loh, N. D.; Matsudaira, P. T.; Mirsaidov, U. Desorption-mediated motion of nanoparticles at the liquid-solid interface. *J. Phys. Chem. C* **2016**, *120*, 20462–20470.
- (34) Gast, A. P.; Russel, W. B. Simple ordering in complex fluids. *Phys. Today* **1998**, *51*, 24–30.
- (35) Li, B.; Wang, F.; Zhou, D.; Peng, Y.; Ni, R.; Han, Y. Modes of surface premelting in colloidal crystals composed of attractive particles. *Nature* **2016**, *531*, 485–488.
- (36) Ronneberger, O.; Fischer, P.; Brox, T. In *U-Net: Convolutional Networks for Biomedical Image Segmentation*, MICCAI International Conference, 2015; pp 234–241.
- (37) Moen, E.; Bannon, D.; Kudo, T.; Graf, W.; Covert, M.; Van Valen, D. Deep learning for cellular image analysis. *Nat. Methods* **2019**, *16*, 1233–1246.

- (38) Yao, L.; Ou, Z.; Luo, B.; Xu, C.; Chen, Q. Machine learning to reveal nanoparticle dynamics from liquid-phase TEM videos. *ACS Cent. Sci.* **2020**, *6*, 1421–1430.
- (39) Steinhardt, P. J.; Nelson, D. R.; Ronchetti, M. Bondorientational order in liquids and glasses. *Phys. Rev. B* **1983**, 28, 784–805.
- (40) Dullens, R. P. A.; Mourad, M. C. D.; Aarts, D. G. A. L.; Hoogenboom, J. P.; Kegel, W. K. Shape-induced frustration of hexagonal order in polyhedral colloids. *Phys. Rev. Lett.* **2006**, *96*, No. 028304.
- (41) Zhao, K.; Bruinsma, R.; Mason, T. G. Local chiral symmetry breaking in triatic liquid crystals. *Nat. Commun.* **2012**, *3*, No. 801.
- (42) Lavergne, F. A.; Aarts, D. G. A. L.; Dullens, R. P. A. Anomalous grain growth in a polycrystalline monolayer of colloidal hard spheres. *Phys. Rev. X* **2017**, *7*, No. 041064.
- (43) Ramananarivo, S.; Ducrot, E.; Palacci, J. Activity-controlled annealing of colloidal monolayers. *Nat. Commun.* **2019**, *10*, No. 3380.
- (44) Lavergne, F. A.; Curran, A.; Aarts, D. G. A. L.; Dullens, R. P. A. Dislocation-controlled formation and kinetics of grain boundary loops in two-dimensional crystals. *Proc. Natl. Acad. Sci. U.S.A.* **2018**, *115*, 6922–6927.
- (45) Li, W.; Peng, Y.; Zhang, Y.; Still, T.; Yodh, A. G.; Han, Y. Shear-assisted grain coarsening in colloidal polycrystals. *Proc. Natl. Acad. Sci. U.S.A.* **2020**, *117*, 24055–24060.
- (46) Pertsinidis, A.; Ling, X. S. Diffusion of point defects in two-dimensional colloidal crystals. *Nature* **2001**, *413*, 147–150.
- (47) Schall, P.; Cohen, I.; Weitz, D. A.; Spaepen, F. Visualization of dislocation dynamics in colloidal crystals. *Science* **2004**, *305*, 1944–1948.
- (48) Lehtinen, O.; Kurasch, S.; Krasheninnikov, A. V.; Kaiser, U. Atomic scale study of the life cycle of a dislocation in graphene from birth to annihilation. *Nat. Commun.* **2013**, *4*, No. 2098.
- (49) Irvine, W. T. M.; Hollingsworth, A. D.; Grier, D. G.; Chaikin, P. M. Dislocation reactions, grain boundaries, and irreversibility in two-dimensional lattices using topological tweezers. *Proc. Natl. Acad. Sci. U.S.A.* **2013**, *110*, 15544–15548.